





Bioinspiration & Biomimetics



PAPER

Flapping dynamics of an inverted flag behind a cylinder

Oluwafemi Ojo¹ , Eetu Kohtanen², Aojia Jiang¹, Jacob Brody² , Alper Erturk²  and Kouros Shoele^{1,*} 

¹ Department of Mechanical Engineering, Joint College of Engineering, Florida A&M University-Florida State University, Tallahassee, FL, United States of America

² G.W. Woodruff School of Mechanical Engineering, Georgia Institute of Technology, Atlanta, GA, United States of America

* Author to whom any correspondence should be addressed.

E-mail: kshoele@eng.famu.fsu.edu

Keywords: piezoelectric, inverted flag, energy harvesting, flag flapping, vortex dynamics

Supplementary material for this article is available [online](#)

RECEIVED
15 June 2022

REVISED
29 August 2022

ACCEPTED FOR PUBLICATION
30 September 2022

PUBLISHED
27 October 2022

Abstract

The inverted flag configuration is inspired by biological structures (e.g. leaves on a tree branch), showing rich dynamics associated with instabilities at lower flow speeds than the regular flag configuration. In the biological counterpart, the arrangement of leaves and twigs on foliage creates a complex interacting environment that promotes certain dynamic fluttering modes. While enabling a large amplitude response for reduced flow speeds is advantageous in emerging fields such as energy harvesting, still, little is known about the consequence of such interactions. In this work, we numerically study the canonical bio-inspired problem of the flow-structural interaction of a 2D inverted flag behind a cylindrical bluff body, mimicking a leaf behind a tree branch, to investigate its distinct fluttering regimes. The separation distance between the cylinder and flag is gradually modified to determine the effective distance beyond which small-amplitude or large-amplitude flapping occurs for different flow velocities. It is shown that the flag exhibits a periodic large amplitude—low frequency response mode when the cylinder is placed at a sufficiently large distance in front of the flag. At smaller distances, when the flag is within the immediate wake of the cylinder, the flag undergoes a high frequency—small amplitude response. Finally, the flag's piezoelectric power harvesting capability is investigated numerically and experimentally for varying geometrical and electrical parameters associated with these two conditions. Two separate optimal response modes with the highest energy output have also been identified.

1. Introduction

The dynamics of a flag in uniform flow have been studied through various experimental [1, 2], numerical [3–7], and analytical [8, 9] techniques. Flag fluttering has also been employed to explore a wide range of biological and engineering applications including fish locomotion [10–13], wing fluttering [14], and energy harvesting [15, 16]. The dynamics of a flag in uniform flow can be categorized into two canonical configurations: (a)—‘regular flag’ defined as the configuration with a fixed leading edge and a free to flap trailing edge and (b)—‘inverted flag’ configuration which is fixed at the trailing edge and has a free-to-move leading edge. When subjected to uniform flow, the flow-induced flapping of flags can be classified into three groups [17]: (a)—instability induced excitation (inverted

flag configuration), (b)—movement-induced excitation (regular flag configuration), (c)—extraneously induced excitation (flag behind a bluff body). The periodic vortex shedding from the deflected position of an inverted flag is the primary factor that drives its sustained flapping dynamics [2, 6, 12]. In contrast, the regular flag dynamics are self-excited due to the dynamic feedback between the flag inertia forces, elastic deflection and fluid forces [18, 19]. For flags behind bluff bodies, vortices shed from the upstream bluff body have a critical effect on the flag dynamics [20].

The response of the inverted flag configuration is distinct from the regular flag. Previous studies have shown that inverted flags become unstable at a much lower critical velocity than regular flags [20] while flags behind a bluff body lose their stability at an even lower critical velocity [21]. Inverted flags

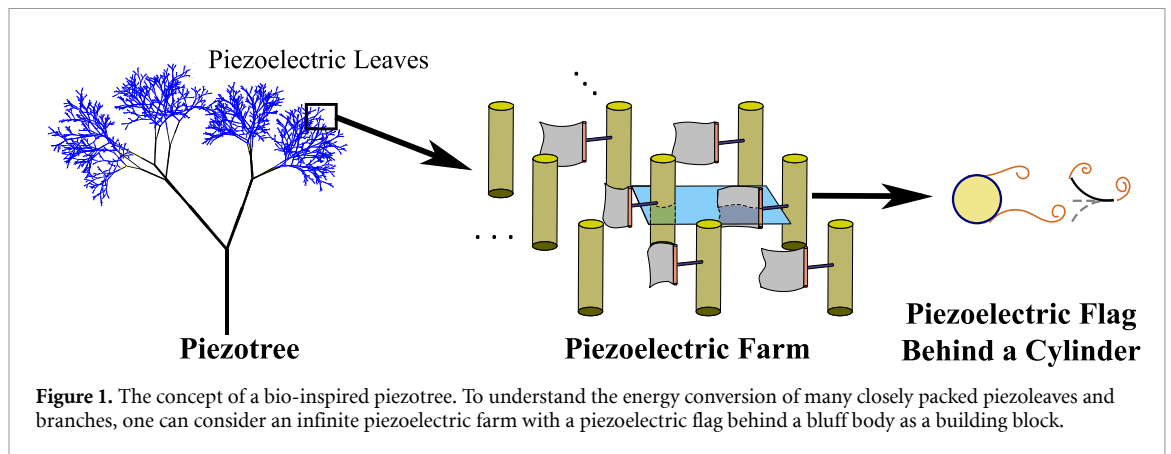


exhibit multiple response modes due to their interaction with flow [4, 22] and their response is highly correlated with the leading-edge vortex separation dynamics [23]. When placed in the wake of a bluff body, the interaction of the bluff body wake and the flag initiates distinct response modes. This includes, but is not limited to, stationary response mode (either undeflected at small flow velocity or deflected at larger flow velocity), small amplitude flapping, and large amplitude flapping modes [21]. These modes generally emerge from the balance between the fluid dynamic forces from the vortex generated from the upstream bluff body, the self-induced flow field, and the internal bending stiffness of the flag, all interconnected based on the flag instability behavior in uniform and perturbed flow conditions.

The dynamic instability of a flag behind a rigid bluff body has recently drawn research interest due to its potential advantages for energy harvesting and bio-inspired locomotion. Allen and Smits [24] observed that the vortices shed by an upstream rectangular plate induce periodic flapping flag motion and can yield the lock-in between the vortex shedding and flapping frequencies. Likewise, vortices shed behind cylindrical bluff bodies can generate different flapping modes in flexible structures. Aquatic animals often leverage vortex shedding from a front bluff body or another live fish to reduce energy expenditure [25, 26]. Fish are shown to coordinate their movement with shed vortices to improve swimming efficiency [27]. The importance of vortices in fish locomotion is also emphasized in the study of Beal *et al* [28], where it was observed that a dead fish continues to swim when it is behind a vortex generating cylinder. At a sufficiently large distance from the cylinder, shed vortices can enhance the thrust and flapping efficiency, while at short distances, the vortices negatively influence the propulsion [29]. Pan *et al* [30] observed that the separation distance and Reynolds number can play a role in the flapping dynamics of flags behind a cylinder.

The fluttering motion of leaves is another biological example where the system's response is influenced by its aerodynamic interaction with the

surrounding branches [31]. Tree branches can act as an upstream vortex generator, amplifying the fluttering behavior of leaves irrespective of variations in wind velocity. On a smaller scale, to understand the rich fluid-structure interaction (FSI) encompassing such systems, the flapping of a flag has been used as an idealized system for studying leaf fluttering dynamics [2, 32].

The performance of the above and many other biological systems are directly linked to their ability to adjust to the surrounding flow. Thus, it is critical to identify their different FSI regimes to encode these interactions into bio-inspired energy harvesting and locomotion applications. One such application considered in this paper is the bio-inspired piezoleaf structure. Here a flexible piezoelectric thin plate (hereafter generally referred to as a piezoelectric flag mimicking a tree leaf) is placed behind a finite-size bluff body representing a tree branch. The knowledge obtained from this study can guide the characterization of a large, closely packed piezofarm. Also, it can eventually lead the way to a bio-inspired design of a piezotree wherein energy is harvested from a self-similar fractal structure similar to a biological tree. The concept and sequences of its building blocks are shown in figure 1.

It is well-documented that the flow-induced vibration of flexible plates/flags can be leveraged for energy harvesting from ambient flow [33–35]. Piezoelectric materials are often employed to transform mechanical energy into electrical energy [36]. One such design is the leaf-inspired piezoelectric wind harvester, in which piezoelectric materials are connected to a flexible plate. Oh *et al* [35] proposed a tree-inspired design concept to harvest energy by embedding polyvinylidene fluoride (PVDF) on leaves on a tree. Subsequently, Nguyen *et al* [37], and Fang *et al* [38] showed that the 'artificial leaf' concept can be employed to capture CO₂ directly and convert it into electricity. The idea of piezoleaves can be extended to concurrently and robustly harvest energy from irregular wind and solar power [33, 34]. While an individual piezoleaf can provide enough

electrical power to drive small sensors & electronic devices, a blue-sky concept is a ‘tree’ with thousands of rationally arranged piezoleaves. These closely spaced piezoleaves incorporate solar cells and harvest energy from the wind as well as the sun to reach a much higher energy production limit. The precursor to such innovation is a better understanding of piezoleaf vibration and energy harvesting in the proximity of other objects.

Piezoelectric flags are shown to be suitable energy harvesters for low energy devices [39–42]. Latif *et al* [43] showed that maximum energy could be harvested for regular flags when the flag is positioned outside the flow suction regime close to the cylinder. Also, Akaydin *et al* [39] observed that maximum power is harvested when the vortex shedding frequency of the cylinder matches the natural frequency of the piezoelectric flag. Shoele and Mittal [15] showed that the inverted flag configuration in a uniform flow is more efficient than the regular flag for piezoelectric energy harvesting due to its high flapping amplitude. The amount of power harvested by a piezoelectric energy harvester is also closely interconnected to the flapping frequency and the oscillation amplitude; both are strongly correlated with the flow field around the flag, especially when the flag is placed near a bluff body with a strong unsteady wake. For example, one can consider an inverted piezoelectric flag oscillating behind a cylinder, where the flag can undergo two vibration modes: high frequency-low amplitude oscillation in the wake or low frequency-large amplitude fluid-elastic fluttering due to leading-edge stall [44]. It is still unknown if the optimal energy can be harvested when the inverted piezoelectric flags undergo small amplitude-high-frequency flapping or when they undergo a large amplitude-low frequency flapping motion outside the wake region.

In this study, we first investigate the mechanisms contributing to the dynamic response of piezoelectric inverted flags subjected to vortex shedding from a cylindrical bluff body. Distinct geometrical properties of the cylindrical bluff body, separation distance (S/L), and the non-dimensional flow speed (U^*) are varied to obtain the flag’s response modes. Then different electrical properties of the piezoelectric flag will be explored numerically and experimentally to predict the response mode associated with the maximum power captured.

2. Numerical formulation and experimental setup

2.1. Governing equations for fluid-structure-electrical coupling of inverted flags

The structural dynamics of the 2D inverted flag without piezoelectricity is governed by the momentum equation written in the flag curvilinear coordinate system ($0 \leq s \leq L$) as Huang and Sung [45], and Shoele and Mittal [15]:

$$m_s \frac{\partial^2 \mathbf{X}}{\partial t^2} = \frac{\partial}{\partial s} \left(\sigma \frac{\partial \mathbf{X}}{\partial s} \right) - \frac{\partial^2}{\partial s^2} \left(\kappa_b \frac{\partial^2 \mathbf{X}}{\partial s^2} \right) - \mathbf{F}, \quad (1)$$

where m_s is the excessive mass of the flag per unit area $(\rho_s - \rho)h_s$ with h_s being the cross-sectional thickness of the flag and ρ_s the flag material density. ρ is the density of the fluid, U is the flow velocity, L is the length of the flag, and κ_b is the flag’s flexural rigidity. σ is the tension in the flag, and \mathbf{F} is the force in the Lagrangian frame exerted on the flag by the fluid. The flag is assumed to be inextensible, and the in-plane tension force σ is determined based on the inextensibility condition of $\mathbf{X}_s \cdot \mathbf{X}_s = 1$.

We assume that the flag surfaces are covered with infinitesimal piezoelectric patches of very small discrete lengths compared to L [42]. Also, the electric circuit is closely coupled with the inverted flag during deformation. The electric voltage of the patches is modified as a result of the charge transfer between the flag surfaces during the stretching or compression of the patches. The piezoelectric patches cover the entire surface of the flag. We denote the electric voltage between the coupled positive electrode of each discrete patch as $V(s, t)$, and the charge per unit length as Q . These electrical quantities are related to the deformation of the flag [15, 42] according to

$$Q(s, t) = cV + \chi \bar{\kappa}, \quad (2)$$

$$\frac{\partial Q}{\partial t} = -gV, \quad \bar{\kappa} = \frac{\partial^2 \mathbf{X}}{\partial s^2} \cdot \mathbf{n}, \quad (3)$$

$$M(s, t) = -\kappa_b \bar{\kappa} + \chi V, \quad (4)$$

where c is the linear capacitance of the piezoelectric element, g is the linear conductivity coefficient between the surfaces of the patches equal to the inverse of the effective resistance between them. The notation $\bar{\kappa}$ is used for the mean curvature at s , χ is the coupling coefficient related to the material properties of the piezoelectric patches and $M(s, t)$ denotes the total internal restoring moment. The Euler–Bernoulli assumption for a slender piezoelectric flag is used to identify the shear force along the length as [46]:

$$\frac{\partial M}{\partial s} = -\kappa_b \frac{\partial}{\partial s} (\bar{\kappa}) + \chi \frac{\partial V}{\partial s}. \quad (5)$$

Here, the first term is the associated with the elastic bending force in equation (1) and the second term is electromechanical coupling force. Finally, the combined non-dimensional structural–electrical equation from (1)–(5) can be written as,

$$\frac{\partial^2 \mathbf{X}}{\partial t^2} = \frac{\partial}{\partial s} \left(\sigma \frac{\partial \mathbf{X}}{\partial s} \right) - \frac{\partial^2}{\partial s^2} \left(\frac{M^*}{U^{*2}} \frac{\partial^2 \mathbf{X}}{\partial s^2} \right) + \frac{\alpha \sqrt{M^*}}{U^*} \left[\frac{\partial}{\partial s} \left(\frac{\partial V}{\partial s} \mathbf{n} \right) \right] - M^* \mathbf{F}, \quad (6)$$

$$\beta \frac{\partial V}{\partial t} = -V - \frac{\alpha \beta \sqrt{M^*}}{U^*} \frac{\partial}{\partial t} (\bar{\kappa}). \quad (7)$$

where similar notations are used for non-dimensional variables as their corresponding dimensional quantities.

The non-dimensional parameters that characterize the coupled structural–electrical equations are listed as:

$$M^* = \frac{\rho L}{m_s}, \quad U^* = UL \sqrt{\frac{\rho L}{\kappa_b}}, \quad \alpha = \frac{\chi}{\sqrt{\kappa_b c}}, \quad \beta = \frac{cU}{gL}. \quad (8)$$

where U^* and M^* quantify the relative importance of the flexibility and inertia of the inverted flag, respectively, while α , and β are the electromechanical coupling and electrical tuning coefficients. The Lagrangian force \mathbf{F} [47, 48] is modeled as the feedback forcing term,

$$\mathbf{F} = \alpha_f \int_0^t (\mathbf{U}_s - \mathbf{U}_f) d\tau + \beta_f (\mathbf{U}_s - \mathbf{U}_f), \quad (9)$$

where \mathbf{U}_f is the interpolated fluid velocity at the surface of the flag, $\mathbf{U}_s = \frac{d\mathbf{x}}{dt}$ is the flag velocity, while α_f and β_f are coefficients used to satisfy the stability criterion, $\alpha_f \Delta t^2 / \Delta s = 0.4$ and $\beta_f = \alpha_f \Delta t$ reported in [48]. A smooth four-points delta kernel function is then used to interpolate the Lagrangian fluid velocity at the flag surface from the Eulerian fluid velocity in the bulk region [49],

$$\mathbf{U}_f(\mathbf{s}, t) = \int_{V_f} \mathbf{u}(\mathbf{x}, t) \delta(\mathbf{X}(\mathbf{s}, t) - \mathbf{x}) d\mathbf{x}, \quad (10)$$

where \mathbf{u} is the non-dimensional flow velocity. Similarly, the Eulerian fluid body force (feedback force density for the FSI) is calculated from the flag's Lagrangian force as,

$$\mathbf{f}(\mathbf{x}, t) = \int_S \mathbf{F}(s, t) \delta(\mathbf{X}(s, t) - \mathbf{x}) ds. \quad (11)$$

The non-dimensional Navier–Stokes momentum and continuity equations for incompressible fluids are the governing equations for the fluid flow and are expressed as:

$$\left[\frac{\partial \mathbf{u}}{\partial t} + \mathbf{u} \cdot \nabla \mathbf{u} \right] = -\nabla p + \frac{1}{\text{Re}} \nabla^2 \mathbf{u} + \mathbf{f}, \quad (12)$$

$$\nabla \cdot \mathbf{u} = 0 \quad (13)$$

p is the dynamic pressure, $\text{Re} = \rho UL / \mu$ is the Reynolds number with μ being the dynamic viscosity.

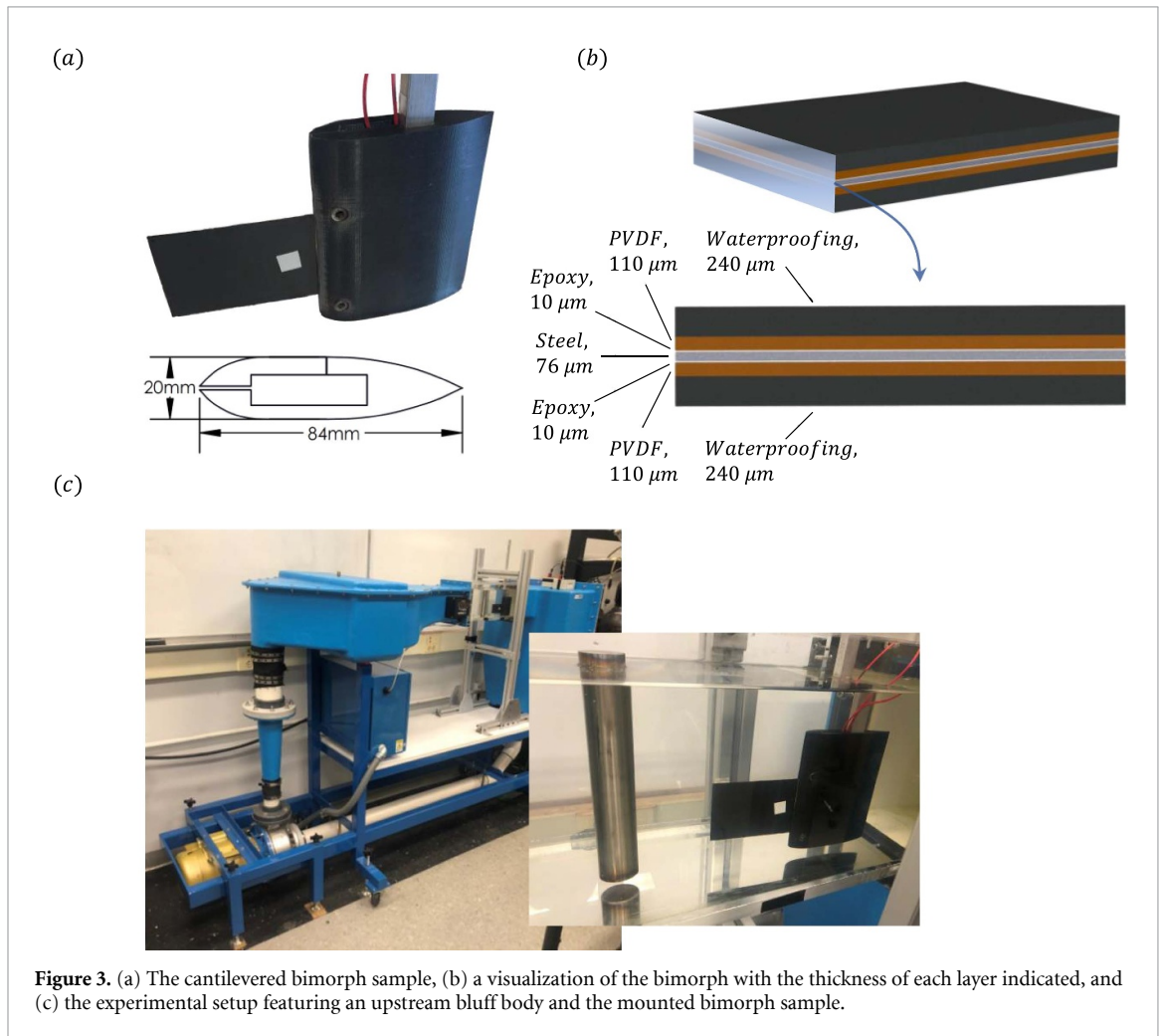
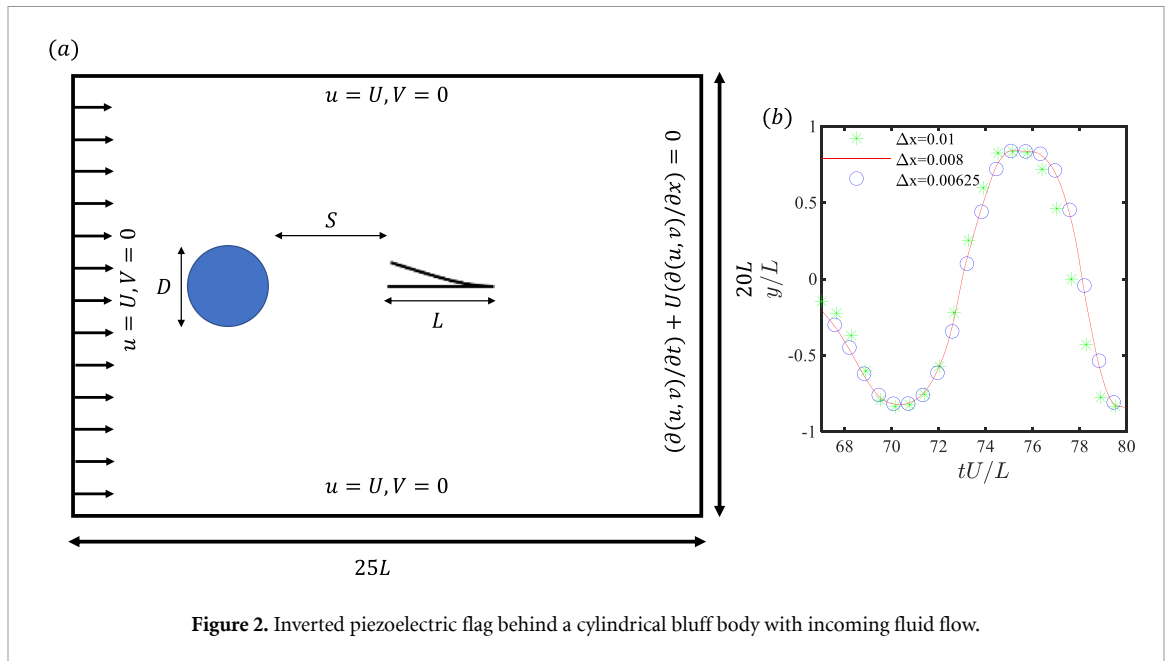
Following Michelin and Doaré [42], and Shoele and Mittal [15], the mean piezoelectric power harvested is calculated from the instantaneous power of the coupled piezo-patches and normalized with the kinetic energy flux around the flag, $\rho U^3 L$, as

$$P_{\text{PIEZO}} = \frac{P}{\rho U^3 L} = \frac{1}{\beta} \int_0^1 V^2 ds. \quad (14)$$

The inverted flag has the following boundary conditions: the fixed boundary is imposed at the trailing edge, and the free boundary condition is implemented at the leading edge. The details of numerical implementation for solving the fluid, structural and electrical equations are described in Shoele and Mittal [15]. The Reynolds number used for the simulation is 600. The mass ratio (M^*) is fixed at five following a sensitivity study to ensure that the model can approximate the response of a submerged piezoplate in the water tunnel experiments conducted here (section 2.2). Also, the upstream cylindrical bluff body is kept stationary in this study. The computational domain size shown in figure 2(a) is fixed at $0 \leq x \leq 25L$, $-10L \leq y \leq 10L$ identified from the domain sensitivity tests. The cylinder is discretized with $\pi D / \Delta s_D$ points, where $\Delta s_D = 0.0045$, while the flag is properly discretized with 147 points, and the fluid grid with 1180×792 points in x and y directions. This grid size is sufficient for convergence as shown in figure 2(b) where different grid sizes ($\Delta x = 0.01, 0.008, 0.00625$), are tested for $U^* = 2.1$, while the ratio of fluid grid size (Δx) and structural grid size (Δs) is kept constant at $\Delta s / \Delta x = 0.8$ following the optimal relation given in [48]. A uniform velocity is assumed at the inlet, and a convective outflow boundary condition is assumed at the outlet. A Neumann boundary condition is imposed for the pressure on all boundaries. The fluid grid spacing of 0.00625 is used for this study. All simulations are performed until all transient responses pass and only after this period, the simulation outputs are used for the calculation of results shown in section 3.

2.2. Experimental setup

A flexible piezoelectric bimorph beam is fabricated for the experimental portion of the study. The bimorph is comprised of a tempered stainless-steel substrate (of thickness $76 \mu\text{m}$), with each side hosting a $110 \mu\text{m}$ PVDF film bonded in vacuum using a thin $10 \mu\text{m}$ layer of a high shear strength epoxy (3M ScotchWeld™ DP460). The vacuum bonding process is described in more detail in [50]. The PVDF film covers the entire area of the steel substrate, with an overhang length of 75 mm and a width of 51 mm in the cantilever configuration. The steel substrate provides a robust series connection for the two PVDF layers, producing an effective capacitance of $C_p = 2.9 \text{ nF}$. The piezoelectric material is waterproofed with multiple thin layers of a flexible rubber coating (Plasti Dip), yielding an average waterproofing thickness of $240 \mu\text{m}$ for each side. Once the sample is waterproofed, it is fixed to a 3D-printed hydrodynamic two-part polylactic acid (PLA) clamp. The clamped bimorph is seen in figure 3(a) with a representative clamp cross section, and an illustration



of the through-thickness components of the bimorph is shown in figure 3(b).

The experiments are performed in a water tunnel manufactured by ELD Inc. with the setup seen in

figure 3(c) at room temperature (20 °C). The water tunnel hosts a square test section measuring 152 mm in directions perpendicular to flow, and 457 mm in the flow direction. The setup features a cylinder

placed at a specified distance upstream from the sample. The considered cylinder diameters are 15 mm and 28.5 mm corresponding to $D/L = 0.20$ and 0.38 , respectively. The voltage from the bimorph is read across a load resistance connected in series. The resistance values are set with an adjustable resistance box and range from $1\text{ M}\Omega$ up to $100\text{ M}\Omega$ for a range of flow speeds between 0.16 m s^{-1} and 0.50 m s^{-1} and $\text{Re} = 14000$ using a high impedance ($>1\text{ G}\Omega$) DAQ (NI 9215). The transverse vibration velocity of the beam is recorded simultaneously at a location 14 mm from the base with a PDV-100 laser Doppler vibrometer. The flow speed is incremented in fine steps of 0.008 m s^{-1} with a 20 s dwell at each speed using an automated script that controls the motor frequency. The average power output is then calculated using the known voltage and load resistance values.

3. Results

The flag behind a cylindrical bluff body shows three response modes when $\text{Re} = 600$: (1)—stationary mode, (2)—small amplitude flapping mode (SAF), and (3)—large-amplitude flapping mode (LAF). These modes strongly depend on the separation distance (S/L) of the flag and cylinder, the diameter of the cylinder (D/L), and the non-dimensional velocity (U^*). When the flag is very close to the cylindrical bluff body ($S = 0.4L$), here at $U^* = 2.1$ (corresponding to a self-oscillatory mode of the flag in uniform incoming flow), it exhibits either the stationary or the SAF modes. As shown in figure 4(a), for small cylindrical diameters $D/L \leq 0.25$, the flag remains stationary with zero amplitude. Here, the flag is trapped within the wake of the cylinder, and the flow remains attached to the cylinder and flag, as shown in figures 5(a) and (b) [30]. For larger cylindrical diameter of $0.30 \leq D/L \leq 0.4$, a coherent vortex street appears in the wake of the cylinder due to an increase in the bluff body diameter. This initiates the forced motion of the flag and results in SAF within the wake, shown in figure 5(c). In this case, two effects contribute to the flag oscillation: the periodic force from the vortex street and flow-induced stiffness due to the motion of the flag in the wake of the cylinder. In particular, there is a finite region immediately behind the cylinder with low pressure and a large pressure gradient in the cross-flow direction. As the flag oscillates across this region, there is an extra flow-induced stiffness that limits the vibration amplitude of the flag and prevents the amplification of SAF to LAF otherwise happening at a larger S/L range. It is observed that the flapping amplitude is influenced by the vortex shedding from the bluff body. Also, the vortex force increases with increasing D/L in this region, as shown in figure 4(a).

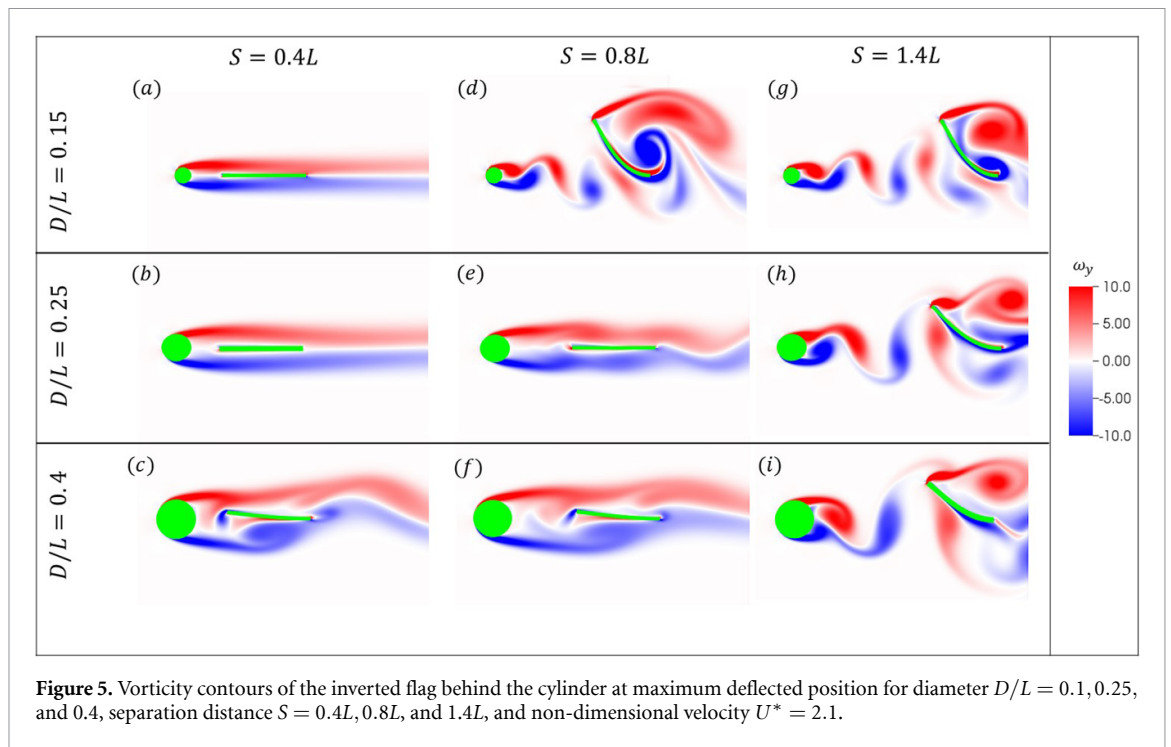
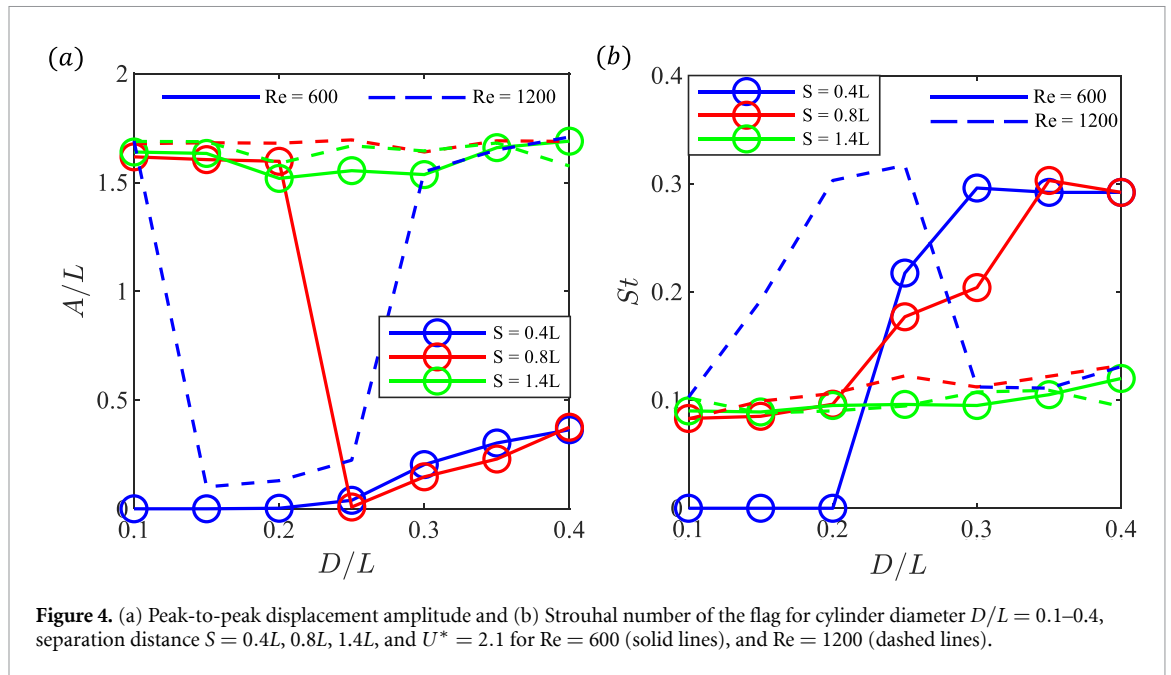
When the flag is placed farther from the cylinder ($S = 0.8L$), it exhibits all three response modes when $\text{Re} = 600$ depending on the size of the bluff

body diameter. When $U^* = 2.1$, for narrow cylinders, $D/L \leq 0.2$, vortices are now periodically shed between the cylinder and the inverted flag as shown in figure 5(d). This is different from what is observed when $S = 0.4L$ for the same configuration, suggesting that beyond an optimal separation distance, the flag has a limited effect on the vortex shedding of the cylinder and regular Kármán vortex street from the bluff body occurs. Here, the energetic vortices kick start the flag's excitation, and the flag exhibits LAF mainly due to its inherent interaction with the flow. The cylinder acts as a triggering front body which essentially cause the flag to start vibrating at smaller U^* value. Beyond this region, at $D/L = 0.25$, the flag reverts to the stationary mode as the bending stiffness of the flag dominates the fluid inertia, as shown in figure 5(e). At $0.30 \leq D/L \leq 0.4$, even if the flag is stiffer, stronger regular vortex pairs are present in the approaching flow to the flag and this induces SAF mode within the wake of the cylinder. The flapping amplitude becomes larger with an increase in the cylinder diameter, as shown in figures 4(a) and 5(f).

At the farthest distance from the bluff body ($S = 1.4L$) when $\text{Re} = 600$ and $U^* = 2.1$, LAF occurs for all the bluff body diameters (D/L) as shown in figure 4(a). Here, the flag is outside the near body low-pressure region and the main mode of the interaction is the leading-edge vortex separation of the inverted flag in the perturbed flow. For all cases, periodic vortex shedding from the cylinder initiates LAF motion and the subsequent flag dynamics is mainly due to its interaction with the flow as shown in figures 5(g)–(i). The flapping amplitude reduces slightly at $0.20 \leq D/L \leq 0.3$ as the approaching flow velocity to the flag reduces and the bending stiffness slightly dominates. When $0.35 \leq D/L \leq 0.4$, the flapping amplitude increases again as more energetic vortices are shed from wider bluff body diameter.

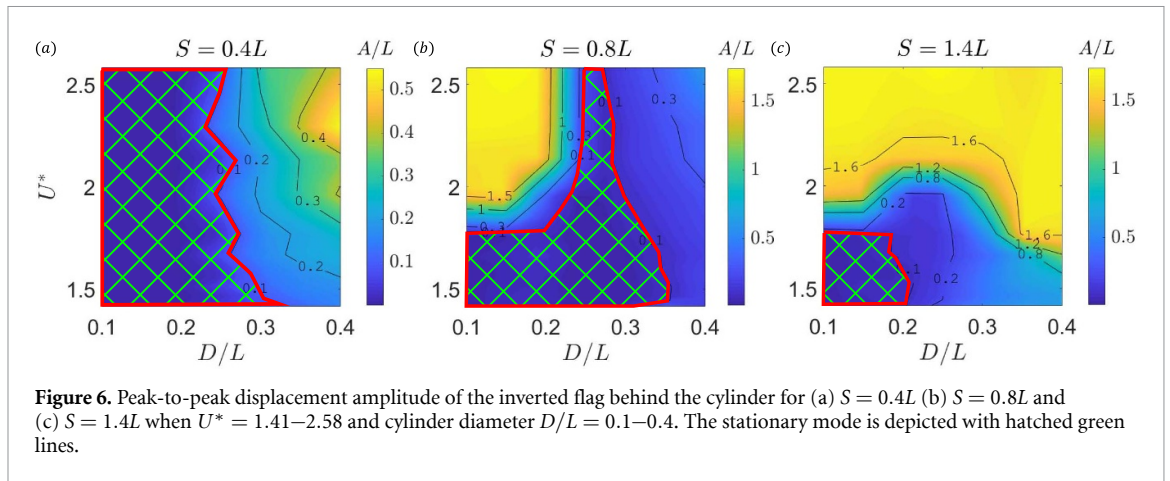
High flapping amplitude does not correspond to high frequency, as shown in figure 4(b), and instead, the reverse trend is the case. The flag experiences its highest Strouhal number ($\text{St} = fL/U$) at the region of SAF for $S = 0.4L$, and $0.8L$ while the flapping frequency is much lower when the flag undergoes LAF. Also, it is observed that St (defined based on the flag's length) increases with increasing bluff body diameter for all cases as anticipated. Given that the scaling of the power capturing of the flag in its first mode of vibration has a linear relation to the vibration amplitude and a quadratic relation to flapping frequency, both SAF and LAF can be potentially good scenarios for piezoelectric energy harvesting. This will be discussed in section 3.3.

For all D/L and S/L cases, we investigate the effect of Re by studying the flapping dynamics of the flag associated with $\text{Re} = 1200$ at $U^* = 2.1$ as shown in figures 4(a) and (b). It is observed that the flag only exhibits the SAF and LAF modes, while the stationary mode does not occur. The results suggest that



increasing Re leads to a more energetic interaction between the vortices in the cylinder’s wake and the flag, thereby eliminating the attached flow behavior and the stationary mode observed previously. Also, an increase in Re reduces the distance where the alternating vortex street forms behind the cylinder. For the smallest separation distance ($S = 0.4L$), the flag exhibits the LAF or SAF modes depending on D/L due to the increased flow unsteadiness. When $D/L = 0.1$, periodic vortex shedding occurs at a shorter distance from the cylinder, thus exciting the flag into the LAF mode. However, as the cylinder diameter increases ($D/L = 0.15$ – 0.25), vortex pairs are

alternatively placed on either side of the flag, inducing SAF in the cylinder’s wake. When $0.3 \leq D/L \leq 0.4$, the flag reverts to the LAF mode as the bluff body induces stronger vortices and pressure fluctuation on the flag. For $S = 0.8L$ and $S = 1.4L$, the increased flow inertia induces periodic vortex shedding from the cylinder, which excites the flag into the LAF mode for all D/L with a slightly larger amplitude as shown in figure 4(a). Also, the same trend of St is observed for $Re = 1200$. The highest St is associated with the SAF mode, while flags that undergo LAF have a relatively lower St as shown in figure 4(b).



3.1. Effect of U^* on the flag's dynamics

The dynamics of an inverted flag in both uniform and perturbed flow conditions is highly dependent on U^* [23]. Here, the non-dimensional velocity is varied from $1.41 \leq U^* \leq 2.58$, while the separation distance is kept constant at representative values of $S = 0.4L, 0.8L, 1.4L$. The cylinder diameter vary between $0.1 < D/L \leq 0.4$. The inverted flag exhibits three major modes over a wide range of U^* . When $S = 0.4L$, for all U^* cases, the flag is either trapped or oscillates within the wake of the cylinder. The flag dynamics is almost independent of U^* as shown in figure 6(a) and instead is a function of vortex shedding by the cylinder. The flag remains stationary for narrow bluff body diameters ($D/L \leq 0.25$) as vortex shedding does not occur. For wider diameters, $0.3 \leq D/L \leq 0.4$, the flag exhibits SAF motion due to stronger vortices shed from the cylinder. Also, as U^* reduces in this range (wide cylinder diameters), the flapping amplitude gradually reduces due to the increase in the flag's internal bending stiffness compared to the fixed fluid dynamic force from the vortex street behind the bluff body. It is also observed that the flapping amplitude slightly increases with increasing cylinder diameter, as shown in figure 6(a).

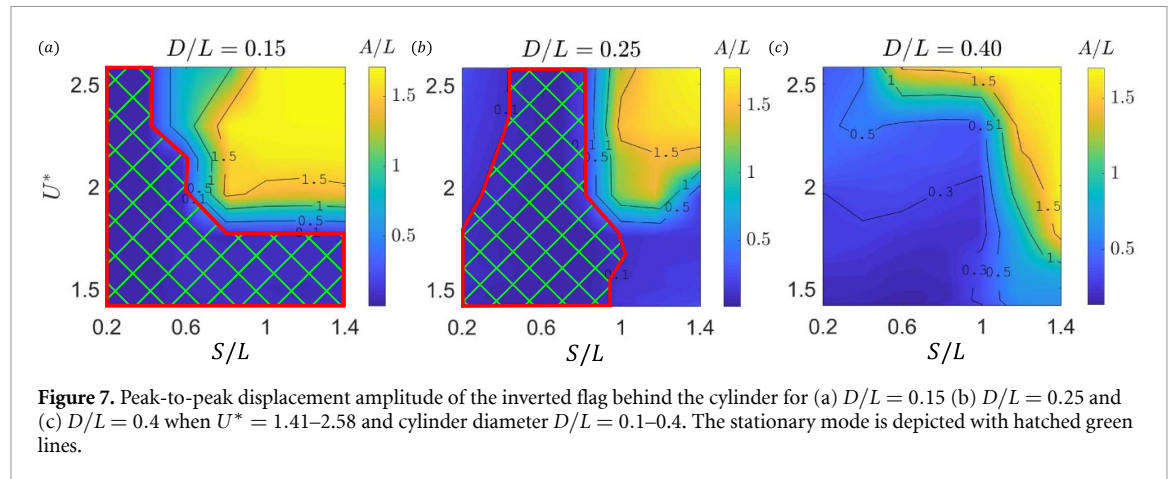
When $S = 0.8L$, the effect of U^* becomes more obvious, as shown in figure 6(b). For $U^* < 1.8$ and $0.1 \leq D/L \leq 0.3$, the flag remains stationary. Though vortex shedding occurs between the flag and the bluff body in this region, the internal bending stiffness of the flag is dominant, thereby preventing the flag from flapping with either a higher amplitude or undergoing SAF motion. For wider cylinder diameters ($0.35 \leq D/L \leq 0.4$) in the same U^* range, the flag undergoes SAF as more energetic vortices are shed. When $U^* > 1.8$, and $D/L \leq 0.2$ the flag kick-starts SAF and the flapping amplitude increases as U^* increases (flow becomes more energetic) until it begins a periodic LAF motion when $U^* \geq 2$. When $U^* > 1.8$, for wider cylinder diameters ($0.3 \leq D/L \leq 0.4$), although the wake is more energetic, vortices are placed on both sides of the flag, which initiates its SAF

motion as shown in figure 5(f). Here, the flag does not bifurcate to LAF as the periodic action of the vortex pairs in the wake controls the growth and separation of the leading-edge vortex of the flag. The flapping amplitude slightly increases with increasing bluff body diameter and U^* in this range. For the particular case of $D/L = 0.25$, the flag remains stationary for all U^* as previously explained.

When $S = 1.4L$, vortex shedding occurs between the flag and the bluff body for all U^* and D/L cases. When $U^* < 1.7$ and $D/L \leq 0.2$, the flag remains stationary and only starts having SAF for larger cylinder diameters ($0.25 \leq D/L \leq 0.4$). The flapping amplitude also increases with increasing D/L as observed in previous cases. When $U^* > 1.7$, the flag first undergoes SAF before transitioning to LAF at higher U^* as shown in figure 6(c). It is also observed that the flapping amplitude slightly decreases when $D/L \approx 0.25$ for $1.7 \leq U^* \leq 2.1$, as previously observed. This result suggests that with small changes in either U^* and/or cylinder size, it would be possible to actuate either SAF or LAF motions for the desired application.

3.2. Effect of S/L on the flag's dynamics

Here, we vary the separation distance between the flag and bluff body to examine the effective distance beyond which SAF or LAF motion occurs. Also, the non-dimensional velocity is varied between $1.41 \leq U^* \leq 2.58$, for three bluff body diameters of $D/L = 0.15, 0.25, 0.4$. When $D/L = 0.15$, the flag remains stationary for $U^* \leq 1.8$ and all separation distances. In this case, there is a stable and extended wake behind the cylinder, which extends the wake shadowing effect to a large distance behind the body. Limited momentum exchange occurs between the free stream and the stable wake of the cylinder; therefore, the leading edge vortex of the inverted flag does not strengthen, and there is no vibration. At $U^* > 1.8$, the flag remains stationary when $S/L < 0.6$, beyond which the flag first exhibits SAF motion for the range of $0.6 \leq S/L < 0.8$. For the larger D/L range,



vortex shedding from cylinder occurs, and the rows of similar sign vortices are convected downstream on both sides of the flag. After this region ($S/L \geq 0.8$), vortex shedding occurs between the cylindrical bluff body and the flag and the wake recaptures most of its kinetic energy due to the action of the vortices. This results in the LAF motion of the flag as shown in figure 7(a). Overall, it is found that the effective distance between the bluff body and flag where LAF occur and vortices are shed between them is $\sim S/L = 0.8$.

For an intermediate cylinder diameter, $D/L = 0.25$, for all U^* and $S/L \leq 0.8$ the flag remains stationary similar to figures 5(b) and (e). In this case, the cylinder diameter is not wide enough to induce a large velocity at the leading edge of the flag and create a leading-edge vortex separation required for SAF. Furthermore, the flag stabilizes the shear layers originating at the cylinder and prevents the Kármán vortex street from forming in front of the flag, which otherwise amplifies the flag oscillation to LAF as observed at larger separation distances. When $S/L \geq 0.8$ and $U^* > 1.8$, periodic vortex shedding now occur with SAF motion when $0.8 \leq S/L < 1$, and LAF when $S/L \geq 1$ and $U^* > 2$ as shown in figure 7(b). The effective separation distance between the bluff body and the flag where LAF occurs is $\sim S/L = 1$.

When the bluff body is wider, for example, $D/L = 0.4$, the flag either exhibits SAF or LAF motion depending on whether the flag is inside or outside the immediate wake region with low pressure. LAF motion occurs for a wider range of separation distance for sufficiently flexible flags (high U^*). In this case, the wake of the cylinder only triggers the initiation of leading-edge vortex separation, while the subsequent vibration of the flag is independent of the cylinder characteristics. The separation distance where LAF motion occurs becomes much larger as U^* reduces as shown in figure 7(c). For other separation distances, the flag undergoes SAF motion. The stationary mode does not occur for wide cylindrical bluff bodies because vortices are strong enough to induce

periodic force on the flag and cause low amplitude oscillation.

In all of the oscillatory cases, it is found that the flag has two stable periodic orbits. The first limit cycle oscillation is from the interaction between the shear layers and vortex separation at the leading edge. The small-amplitude oscillation of the flag stabilizes the shear layer. In this case, the leading edge vortex separation is in the opposite direction of the flag oscillation and creates a restoring force on deflecting flag. In the second limit cycle response, the cylinder only creates the perturbation necessary for the flag to initiate its large amplitude fluttering motion. During this condition, the oscillation of the flag is self-driven, caused by the initiation and strengthening of the leading-edge vortex. During each cycle, the leading edge vortex separation happens in the direction of the flag motion, and the oscillation is driven by the interaction between the leading and trailing edge vortices of the flag.

3.3. Piezoelectric energy harvesting

We now examine the power harvested in the inverted flag when $S = 0.8L$. Also, two-cylinder diameters are numerically simulated to show the energy captured in the low frequency LAF region ($D/L = 0.2$) when vortices are shed between the flag and the cylinder and high frequency SAF region in the wake ($D/L = 0.4$). The mean piezoelectric power harvested (P_{PIEZO}) is calculated for varying electromechanical coupling coefficient $\alpha = 0.1$ – 0.5 , electrical resistivity $\beta = 0.1$ – 10 , and $U^* = 1.41$ – 2.2 .

3.3.1. Low electromechanical coupling ($\alpha = 0.1$)

When $\alpha = 0.1$, the piezoelectric patches are loosely coupled with the flag through its flapping cycle. For $U^* = 1.41$ – 1.8 , when $D/L = 0.2$, lower piezoelectric power is harvested as the flag undergoes SAF. At higher velocity $U^* > 1.8$, as the flag undergoes LAF motion, higher power is harvested. It is observed that P_{PIEZO} increases with increasing electrical resistivity up to $\beta = 1$, which corresponds to similar resistive

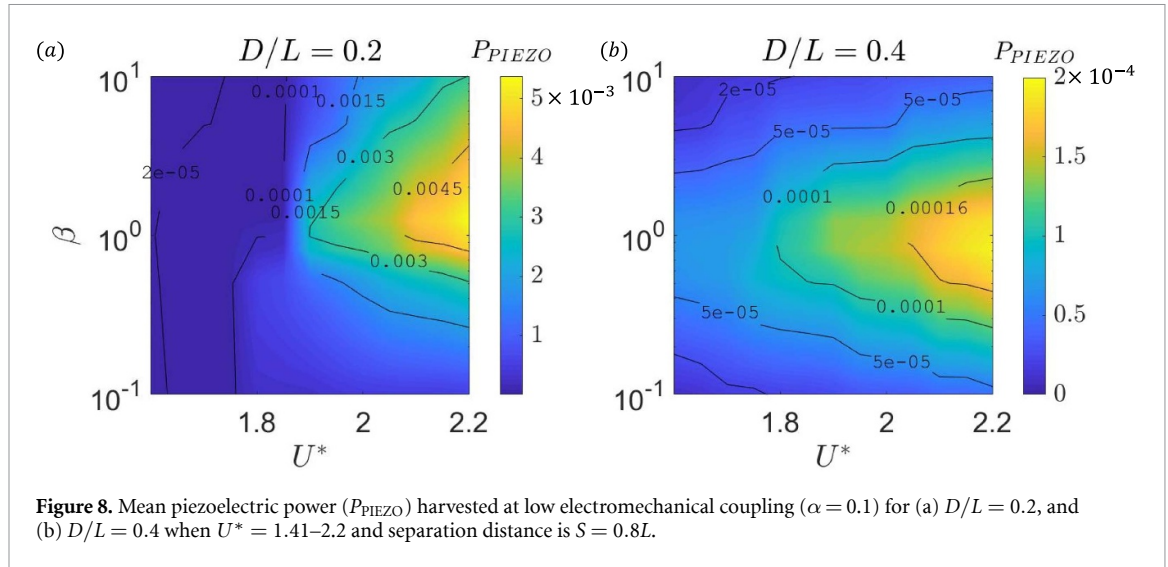


Figure 8. Mean piezoelectric power (P_{PIEZO}) harvested at low electromechanical coupling ($\alpha = 0.1$) for (a) $D/L = 0.2$, and (b) $D/L = 0.4$ when $U^* = 1.41$ – 2.2 and separation distance is $S = 0.8L$.

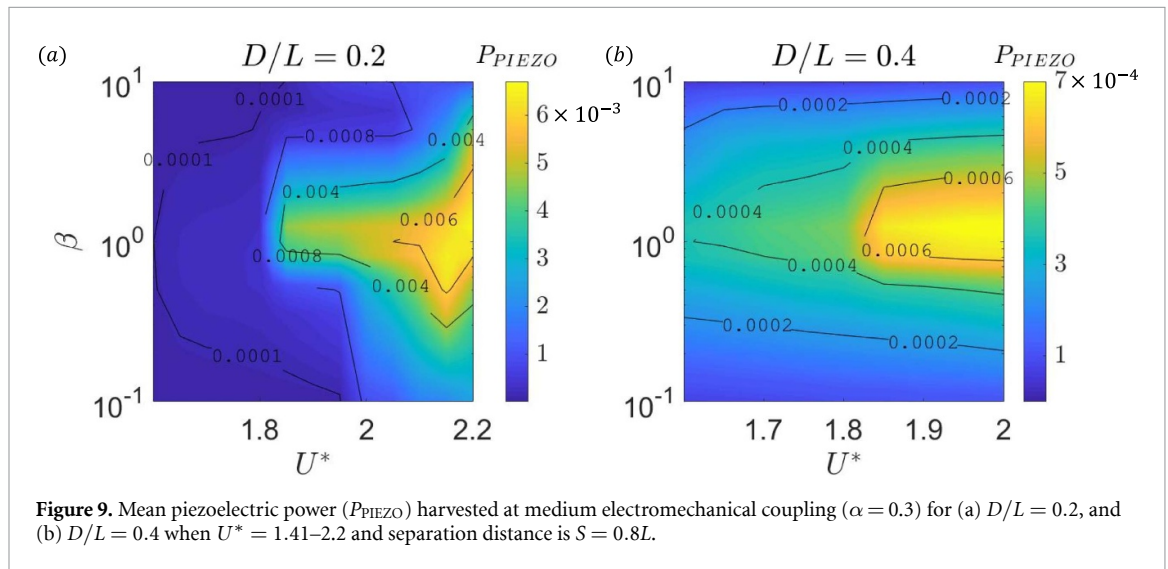


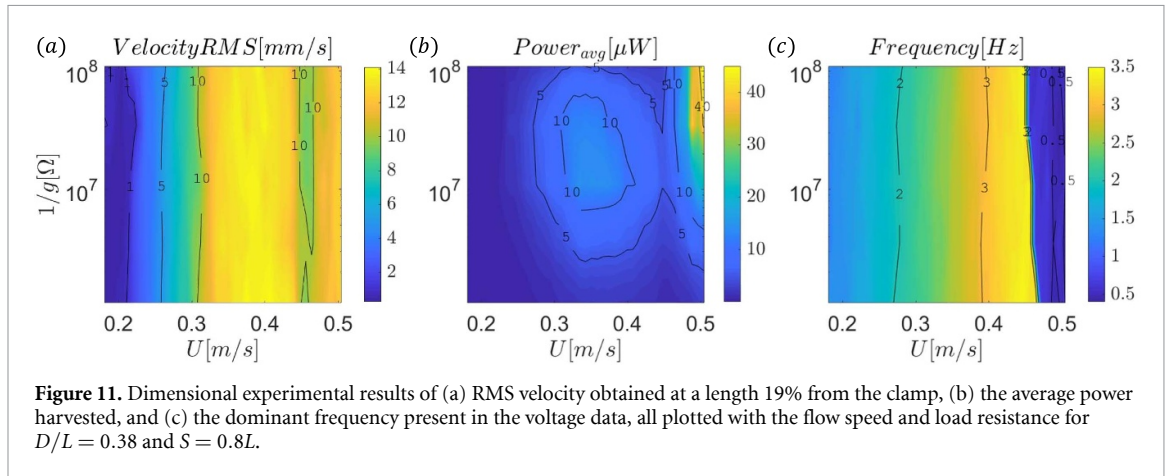
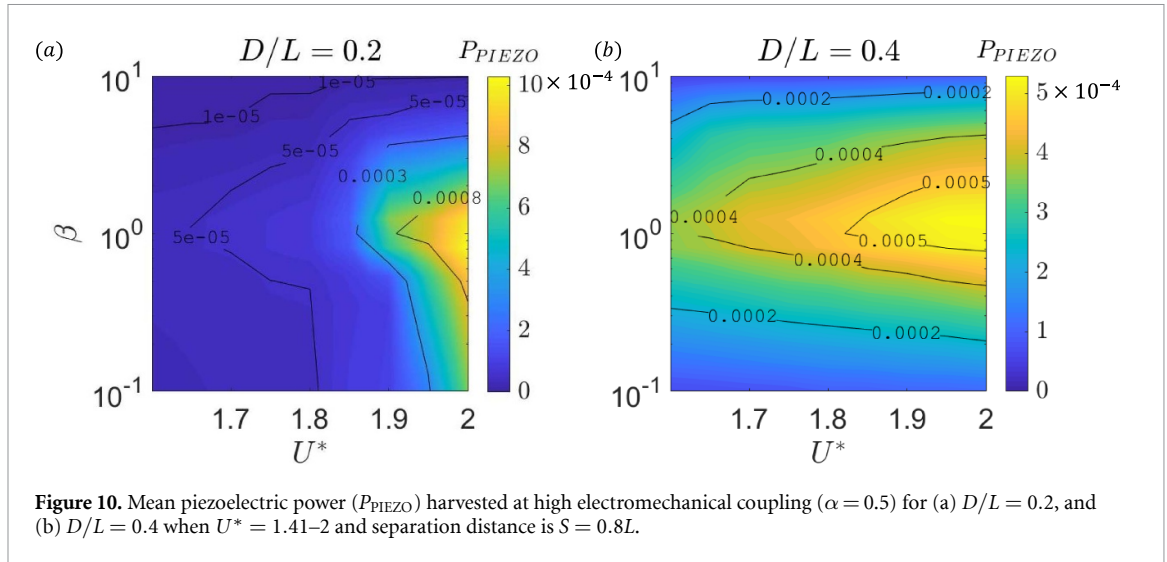
Figure 9. Mean piezoelectric power (P_{PIEZO}) harvested at medium electromechanical coupling ($\alpha = 0.3$) for (a) $D/L = 0.2$, and (b) $D/L = 0.4$ when $U^* = 1.41$ – 2.2 and separation distance is $S = 0.8L$.

and convective timescale of the flow over the flag. Beyond this, an increase in electrical resistivity has a limiting effect on the total harvested power, suggesting that $\beta = 1$ is the most efficient electrical resistivity in the LAF regime. Also, it is observed that P_{PIEZO} increases with increasing U^* , as the highest power is obtained at $U^* \geq 2.1$. When $D/L = 0.4$, for all U^* , the flag undergoes a high frequency SAF motion. Here, P_{PIEZO} also increases with increasing electrical resistivity before decreasing at higher β values as shown in figure 8(b). Higher P_{PIEZO} is also captured as U^* increases for all β cases. Overall, the highest power is associated with the large-amplitude low-frequency region ($D/L = 0.2$), which indicates that an increase in amplitude influences the harvested piezoelectric power more than an increase in flapping frequency.

3.3.2. Moderate electromechanical coupling ($\alpha = 0.3$)
 When the piezoelectric patch is closely coupled with the flag ($\alpha = 0.3$), higher P_{PIEZO} is harvested for all parameters with small feedback on the dynamics of

the flag. For $D/L = 0.2$ and $1.41 \leq U^* \leq 1.9$, lower piezoelectric power is harvested as the internal bending stiffness effect dominates the fluid force and the flag undergoes SAF. When $U^* > 1.9$, it is also observed that for all β values, P_{PIEZO} increases as the flow becomes more energetic and LAF occurs (i.e. as U^* increases) as shown in figure 9(a). Also, β follows the same trend as the previous case with an increasing value of P_{PIEZO} up to $\beta = 1$, and a reduction in power captured at higher β values. When $D/L = 0.4$, only SAF occurs, and P_{PIEZO} increases with U^* . Also, $\beta = 1$ is the optimal electrical resistivity following previous trends as shown in figure 9(b).

3.3.3. High electromechanical coupling ($\alpha = 0.5$)
 Here the piezoelectric patch is tightly coupled with the flag, thereby modifying the flag dynamics. The flag only exhibits its response modes at $U^* < 2$ for all electrical parameters. At higher velocity, flag instability occurs due to the high mismatch in the stiffness of the piezo-patch and flag. Here, the P_{PIEZO} follows the same trend as in previous cases as $U^* > 1.9$ and

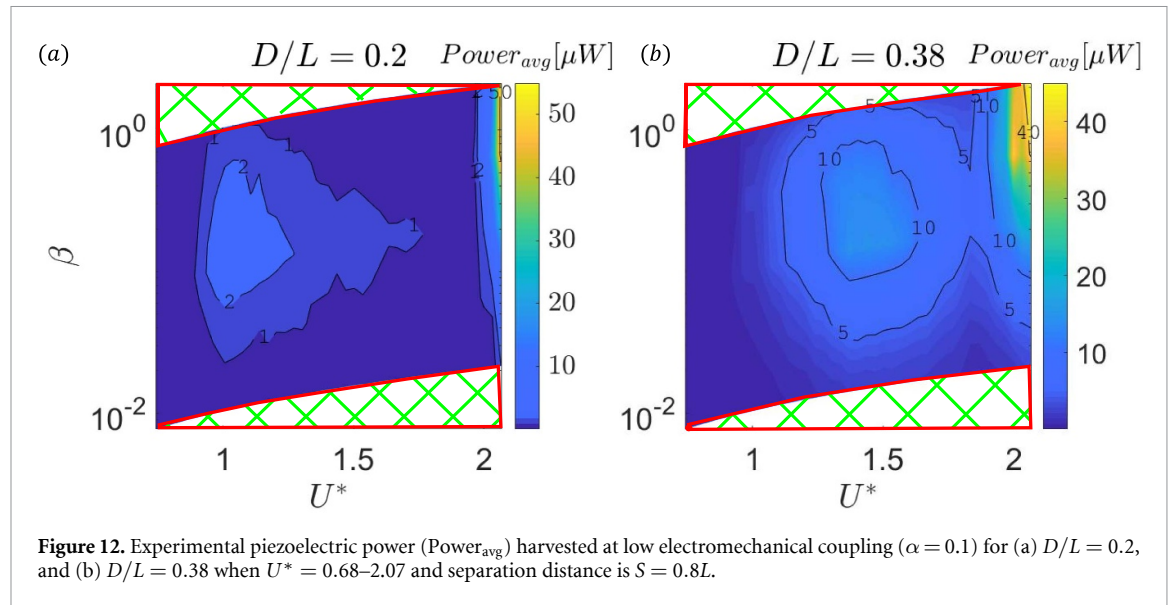


$\beta = 1$ are the most optimal parameter. However, for both cylinder diameters, a reduction in the overall harvested power occurs when compared with $\alpha = 0.3$ as shown in figures 10(a) and (b). This occurs because an increase in α induces extra stiffness on the flag, which modifies its flapping dynamics and reduces the flag's flapping amplitude, thereby reducing the piezoelectric power harvested. Overall, the highest power is captured when $\alpha = 0.3$ for $D/L = 0.2$ and $D/L = 0.4$.

3.4. Comparison with experiments

In order to obtain physical intuition about the behavior of the inverted flag, dimensional experimental results, including the velocity, the average power, and the dominant frequency present in the voltage signal, are plotted against the flow speed and load resistance in figures 11(a)–(c), respectively. The PVDF-based piezoelectric flag used in the experiments has a low electromechanical coupling of $\alpha = 0.1$, making the structural response insensitive to the load resistance. This is confirmed in figure 11(a), where the load resistance is observed not to influence the structural motion. Overall, the trend in

the velocity is non-monotonic with flow speed, with two local maxima observed near $U = 0.38 \text{ m s}^{-1}$ and $U = 0.50 \text{ m s}^{-1}$. The maximum at $U = 0.38 \text{ m s}^{-1}$ corresponds to the SAF regime where the vortex shedding frequency from the cylinder matches the structural resonance frequency. Further increments in flow speed yield a decreasing structural velocity due to the vortex shedding frequency increasing above the structural resonance up to $U = 0.45 \text{ m s}^{-1}$. Past this flow speed, the dynamics of the system transition from SAF to LAF, causing the structural oscillation velocity to increase again with U . The two maxima corresponding to the SAF and LAF regimes are also distinct in the average power in figure 11(b), with respective average power outputs of $14 \mu W$ and $45 \mu W$. Note that, in the SAF regime, the structural response frequency is governed by the vortex shedding frequency that increases monotonically with flow speed, as seen in figure 11(c) for low U . When the flag begins LAF motion near $U = 0.45 \text{ m s}^{-1}$, the structural response is no longer dominated by the vortex shedding frequency; instead, the flag undergoes a low frequency and a high amplitude deflection that extends beyond the wake of the cylinder. These differences in



the structural response frequency cause the optimum load resistance in figure 11(b) to shift from roughly $20\text{ M}\Omega$ for $U = 0.38\text{ m s}^{-1}$ to above $100\text{ M}\Omega$ for $U = 0.50\text{ m s}^{-1}$ per the first order optimal circuit load expression $R_{opt} = 1/(\omega C_p)$ [36].

The experimental average power is also shown in figures 12(a) and (b) for $D/L = 0.20$ and $D/L = 0.38$, respectively, with the dimensionless quantities U^* and β . Note that experimentally U^* is incremented by changing the physical flow speed while β is adjusted by changing the load resistance. Because β depends on both load resistance and flow speed, the non-dimensional experimental results for P_{PIEZO} yield a curved surface. The power output here contains the same optima as observed in the analogous dimensional figure in figure 11(b)—a local optimum power output is present at a relatively low U^* in SAF (near 1.0 for $D/L = 0.20$ and 1.4 for $D/L = 0.38$), whereas higher power is observed near $U^* = 2$ in LAF for both cylinder diameters. In the SAF case, the vibration of the beam is constrained within the wake of the cylinder akin to figure 5(f), for example—for the wider cylinder case of $D/L = 0.38$, the beam's deflection levels are larger, which leads to higher power output than the $D/L = 0.20$ case. The average power in LAF is similar for both cylinders.

The numerical results for the case with low electromechanical coupling in figure 8 are qualitatively similar to the experimental results in figure 12; for each case, the highest power output is observed near $U^* = 2$ and $\beta = 1$. Certain dissimilarities are also present due to differences in the experimental and numerical setups. For example, the maximum experimental power for both $D/L = 0.20$ and $D/L = 0.38$ is of similar magnitude, whereas numerically, the flag behind the narrow cylinder ($D/L = 0.20$) has a much higher maximum power than its wide cylinder counterpart. This is because LAF was not observed numerically for wider cylindrical bluff bodies (e.g.

$D/L = 0.4$) at $S = 0.8L$ and $Re = 600$, where the flag flaps within the wake of the cylinder. The difference in the response mode at this D/L and S/L is due to the higher Reynolds number of the experiment. It is shown in section 3 (figure 4(a)) that at $U^* = 2.1$ and $S = 0.8L$, an increase in Re causes more energetic interactions between the shed vortices and the flag, which induces LAF motion for flags behind wider cylinders. The higher experimental Re and more intense vortex shedding by the cylinder result in higher flapping amplitude of the flag for wider D/L values than those observed numerically, ultimately leading to similar maximum power for both $D/L = 0.20$ and $D/L = 0.38$ experimentally. Overall, the highest piezoelectric power is harvested when the flag undergoes large-amplitude flapping motion for U^* above 2 and β near unity, which is consistent both experimentally and numerically.

4. Conclusion

We studied the dynamics of a flag behind a cylindrical bluff body and observed that its flapping modes strongly depend on the separation distance between the flag and the cylinder, the non-dimensional reduced velocity, and the cylinder diameter. For a small separation distance, the flag is trapped in the cylinder wake when $Re = 600$. Also, when the cylinder diameter is small, the cylinder wake remains steady, and the flag stays in its stationary mode. As the cylinder diameter increases, the vortex pair sheds farther from the cylinder on both sides of the flag, inducing a small-amplitude high-frequency flapping motion. The flapping amplitude also increases as cylinder diameter increases in this range. Large-amplitude flapping occurs when the flag is set farther downstream, and the periodic Kármán vortices are shed between the flag and the cylinder for smaller cylinder diameters. U^* has a more significant

effect in this regime as the periodic large-amplitude flapping of the flag is only obtained at higher reduced velocities. As the cylinder diameter increases, the flag reverts to the small amplitude high-frequency vibration mode within the cylinder wake extent. At a higher separation distance, the flag flaps with a large amplitude for a wider range of velocities. When $Re = 1200$, the flag does not exhibit the stationary mode for all cylinder diameters and separation distance due to increased flow inertia. Only a small or large amplitude flapping motion is obtained here.

The harvested piezoelectric power depends on the flag's response modes. Experiments using a piezoelectric flag with low electromechanical coupling showed trends similar to the corresponding numerical results. It is observed both experimentally and numerically that higher power is harvested when the flag undergoes large amplitude low-frequency vibrations than small-amplitude high-frequency vibrations in the cylinder wake. This suggests that the amplitude is a more crucial factor than the flapping frequency in enhancing piezoelectric power harvesting. It is also found that $\alpha = 0.3$ is the most efficient electromechanical coupling. Beyond that, a higher coupling coefficient induces extra stiffness, modifying the flag's flapping amplitude and reducing the harvested piezoelectric power. Also, the harvested power increases with increasing U^* numerically. It is found that $\beta = 1$ is the most efficient electrical resistance for all cases wherein the resistive timescale is approximately similar to the convective timescale of the flow over the flag.

It is worth mentioning that while the flag's large amplitude vibration is directly associated with a more significant power capture, this dynamic mode might not be optimal for a piezofarm wherein multiple piezoelectric plates are closely placed next to each other, as discussed in the introduction. In a farm setup, the distribution of power capturing between rows of the farm should be adjusted such that some frontal flags flap with a small amplitude to allow the energetic flow penetrates inside the farm while simultaneously maximizing the overall harvested energy. Then, combining small and large amplitude vibration modes can be more effective in reaching an optimal arrangement. The optimum electrical, structural, and geometrical parameters identified in this study (single piezoleaf-branch interaction) can be leveraged toward forming a surrogate model for the design and quantification of a piezofarm with multiple closely packed piezoelectric flags and cylinders for optimal power production from the whole group. Eventually, the identified response modes can be leveraged into a more complex yet sustainable energy harvesting concept of a piezotree with a collection of many leaves and branches to harvest maximum piezoelectric power near roads and inside densely populated areas built environments [51, 52].

Data availability statement

All data that support the findings of this study are included within the article (and any supplementary files).

Acknowledgments


The authors acknowledge NSF-XSEDE for the computational resources through CTS200043 Project on which these simulations were carried out.

Funding

This work is supported by NSF Grant CBET-1943810.

ORCID iDs

Oluwafemi Ojo  <https://orcid.org/0000-0002-8798-8861>

Jacob Brody  <https://orcid.org/0000-0003-0511-3752>

Alper Erturk  <https://orcid.org/0000-0003-0110-5376>

Kouros Shoele  <https://orcid.org/0000-0003-2810-0065>

References

- [1] Eloy C, Kofman N and Schouveiler L 2012 *J. Fluid Mech.* **691** 583–93
- [2] Kim D, Cossé J, Cerdeira C H and Gharib M 2013 *J. Fluid Mech.* **736** R1
- [3] Tang C, Liu N-S and Lu X-Y 2015 *Phys. Fluids* **27** 073601
- [4] Goza A, Colonius T and Sader J E 2018 *J. Fluid Mech.* **857** 312–44
- [5] Solano T, Ordonez J C and Shoele K 2020 *J. Fluid Mech.* **895** A8
- [6] Ojo O, Tan D, Wang Y C, Shoele K and Erturk A 2019 Aspect ratio effects in wind energy harvesting using piezoelectric inverted flags *Proc. SPIE* **10967** 109670Q
- [7] Ojo O, Shoele K, Erturk A, Wang Y C and Kohtanen E 2021 Numerical and experimental investigations of energy harvesting from piezoelectric inverted flags *AIAA Scitech 2021 Forum* p 1323
- [8] Tavallaeejad M, Legrand M and Paidoussis M P 2020 *J. Sound Vib.* **467** 115048
- [9] Sader J E, Huertas-Cerdeira C and Gharib M 2016 *J. Fluid Mech.* **809** 873–94
- [10] Lighthill J 1975 *Aerodynamic aspects of animal flight Swimming and Flying in Nature* (Berlin: Springer) pp 423–91
- [11] Shoele K and Zhu Q 2012 *J. Fluid Mech.* **693** 402–32
- [12] Shoele K and Zhu Q 2013 *Phys. Fluids* **25** 041901
- [13] Michelin S and Llewellyn Smith S G 2009 *Phys. Fluids* **21** 071902
- [14] Tang D, Yamamoto H and Dowell E 2003 *J. Fluids Struct.* **17** 225–42
- [15] Shoele K and Mittal R 2016 *J. Fluid Mech.* **790** 582–606
- [16] Orrego S, Shoele K, Ruas A, Doran K, Caggiano B, Mittal R and Kang S H 2017 *Appl. Energy* **194** 212–22
- [17] Paidoussis M P 1998 *Fluid-Structure Interactions: Slender Structures and Axial Flow* vol 1 (New York: Academic)
- [18] Alben S and Shelley M J 2008 *Phys. Rev. Lett.* **100** 074301
- [19] Shelley M J and Zhang J 2011 *Annu. Rev. Fluid Mech.* **43** 449–65

- [20] Yu Y, Liu Y and Amandolese X 2019 *Appl. Mech. Rev.* **71** 010801
- [21] Kim H, Kang S and Kim D 2017 *J. Fluids Struct.* **71** 1–14
- [22] Tavallaeinejad M, Paidoussis M P, Salinas M F, Legrand M, Kheiri M and Botez R M 2020 *J. Fluid Mech.* **904** R5
- [23] Ojo O, Wang Y-C, Erturk A and Shoele K 2022 *J. Fluid Mech.* **942** A4
- [24] Allen J and Smits A 2001 *J. Fluids Struct.* **15** 629–40
- [25] Weihs D 1973 *Nature* **241** 290–1
- [26] Liao J C 2007 *Phil. Trans. R. Soc. B* **362** 1973–93
- [27] Liao J C, Beal D N, Lauder G V and Triantafyllou M S 2003 *Science* **302** 1566–9
- [28] Beal D, Hover F, Triantafyllou M, Liao J and Lauder G V 2006 *J. Fluid Mech.* **549** 385–402
- [29] Shao X, Pan D, Deng J and Yu Z 2010 *Phys. Fluids* **22** 111903
- [30] Pan D, Shao X, Deng J and Yu Z 2014 *Eur. J. Mech. B* **46** 17–27
- [31] Tadriss L, Saudreau M, Hémon P, Amandolese X, Marquier A, Leclercq T and De Langre E 2018 *J. R. Soc. Interface* **15** 20180010
- [32] Sader J E, Cossé J, Kim D, Fan B and Gharib M 2016 *J. Fluid Mech.* **793** 524–55
- [33] Silva-Leon J, Cioncolini A, Nabawy M R A, Revell A and Kenneough A 2019 *Appl. Energy* **239** 846–58
- [34] Cioncolini A, Nabawy M R A, Silva-Leon J, O’connor J and Revell A 2019 *Fluids* **4** 87
- [35] Oh S, Han H, Han S, Lee J and Chun W 2010 *Int. J. Energy Res.* **34** 431–7
- [36] Erturk A and Inman D J 2011 *Piezoelectric Energy Harvesting* (New York: Wiley)
- [37] Nguyen P D, Duong T M and Tran P D 2017 *J. Sci.: Adv. Mater. Devices* **2** 399–417
- [38] Fang L H, Rahim R A and Naimah S 2021 Design of artificial piezo-leaf wind energy harvesting system monitoring based on Blynk apps *AIP Conf. Proc.* **2339** 020005
- [39] Akaydin H D, Elvin N and Andreopoulos Y 2010 *J. Intell. Mater. Syst. Struct.* **21** 1263–78
- [40] Doaré O and Michelin S 2011 *J. Fluids Struct.* **27** 1357–75
- [41] Akcabay D T and Young Y L 2012 *Phys. Fluids* **24** 054106
- [42] Michelin S and Doaré O 2013 *J. Fluid Mech.* **714** 489–504
- [43] Latif U, Uddin E, Abdullah C, Ali Z, Sajid M, Akhtar K and Shah S R 2020 *J. Renew. Sustain. Energy* **12** 033301
- [44] McCroskey W J 1981 The phenomenon of dynamic stall *Technical Report*
- [45] Huang W-X and Sung H J 2010 *J. Fluid Mech.* **653** 301–36
- [46] Audoly B and Pomeau Y 2010 *Elasticity and Geometry: From Hair Curls to the Non-Linear Response of Shells* (Oxford: Oxford University Press)
- [47] Goldstein D, Handler R and Sirovich L 1993 *J. Comput. Phys.* **105** 354–66
- [48] Vahab M, Sussman M and Shoele K 2021 *J. Comput. Phys.* **429** 110008
- [49] Peskin C S 2002 *Acta Numer.* **11** 479–517
- [50] Anton S, Erturk A and Inman D 2010 *Smart Mater. Struct.* **19** 115021
- [51] McCloskey M A, Mosher C L and Henderson E R 2017 *PLoS One* **12** e0170022
- [52] Kim H S, Kim J-H and Kim J 2011 *Int. J. Precis. Eng. Manuf.* **12** 1129–41